Lab on a Chip

Cite this: *Lab Chip*, 2012, **12**, 4702–4708

www.rsc.org/loc

PAPER

Low cost integration of 3D-electrode structures into microfluidic devices by replica molding†

Benjamin Mustin*[a] and Boris Stoeber[b]

Received 28th June 2012, Accepted 29th August 2012
DOI: 10.1039/c2lc40728k

We demonstrate a new replica molding method for integrating 3D-composite electrodes into microfluidic devices made from polydimethylsiloxane (PDMS) at low cost. Our process does not require work in a cleanroom, expensive materials, or expensive equipment once a micro mold has been fabricated using standard multilayer SU-8 photolithography. Different device geometries have been fabricated to demonstrate the capabilities and limitations of the method. The electrical properties of the composite electrode material are characterized. Furthermore, a device for concentrating particles *via* AC-dielectrophoresis is presented as an example for a potential application of the fabrication process.

1 Introduction

Methods for integrating microscopic conductive features into microfluidic devices are of great importance for the lab on a chip community.[1–3] These features can serve as electrodes for the generation of electric fields, with applications including sample concentration,[4,5] sample separation,[6,7] electrochemical measurements,[8] mixing,[9] electroporation[10,11] and electro-fusion of cells.[12] Conductive features on a chip are also used for generating magnetic fields,[13,14] as well as for temperature sensors[15] and electrical heaters.[15,16] The latter ones find applications in flow control[16] and mixing.[17]

A large variety of approaches for integrating electrodes in microfluidic devices already exists. It is possible to distinguish between thin-film features (typically 100–200 nm thick) that cover one wall of a channel and thicker structures. One of the most commonly used methods for integrating thin conductive features onto a chip is to pattern a substrate (*e.g.* glass slide) with a metal such as gold or silver, while these metals are typically deposited using an (e-beam) evaporator or a sputter deposition tool, both of which are expensive pieces of equipment that require experienced users for their operation. Excess metal is then removed using either a lift-off process or an etching process in combination with standard photolithography methods. More recently, wet chemical methods have been applied to deposit silver on the substrates instead of using e-beam evaporation or sputtering. Subsequent photolithography and wet etching steps are then used to create micron sized conductive features on glass substrates.[18,19] A technical difficulty associated with the methods discussed above is the alignment of fluidic channels on one substrate to electrodes on a second substrate.[20] Alignment is especially difficult when microfluidic devices are made from polydimethylsiloxane (PDMS). The PDMS device is bonded to the patterned substrate containing the electrodes and alignment of the fluidic channels to the electrodes is typically performed by hand. This procedure is often associated with significant alignment errors. Furthermore, fluid leakage can occur in regions close to the electrodes as the PDMS device does not conform perfectly to the patterned substrate and it may not bond to the electrode material.[20] However, these technical difficulties can be overcome and the methods for integrating thin electrodes into microfluidic devices are widely used. Thicker 3-dimensional (3D) electrode structures can be produced by patterning a substrate with thin metal electrodes as described above and subsequent electrodeposition of copper,[21] gold[22,23] or silver.[10] Thick electrode structures have also been made from doped silicon using the four-step process described by Iliescu *et al.*,[24] or from carbon through carbonization of SU-8 photo resist.[25,26] Metal ion implantation has been utilized for integrating sidewall electrodes made from gold into microfluidic channels.[27]

More recently, composite materials consisting of conductive particles dispersed in a PDMS matrix have been utilized as material for thick conductors in microfluidic devices.[28] Nanoparticles such as carbon black,[29] carbon nanotubes,[30] silver nanoparticles,[31,32] copper flakes[33] or nickel nanoparticles[34] are typically premixed with PDMS before the composite is integrated into microfluidic devices using standard photolithography methods. These PDMS composites can show piezoresistive behavior.[30,35] Their conductivity is typically several orders of magnitude lower compared to the conductivity of the bulk particle material and it increases with increasing solid concentration of particles. However, the viscosity also increases

[a]*The University of British Columbia, 2054-6250 Applied Science Lane, Vancouver, BC V6T 1Z4, Canada. E-mail: mustin@mech.ubc.ca; Fax: +1 604 822-2403; Tel: +1 604 827-4593*
[b]*The University of British Columbia, 2054-6250 Applied Science Lane, Vancouver, BC V6T 1Z4, Canada. E-mail: boris.stoeber@ubc.ca; Fax: +1 604 822-2403; Tel: +1 604 827-5907*
† Electronic supplementary information (ESI) available. See DOI: 10.1039/c2lc40728k

drastically with increasing particle concentration,[35,36] so that mixing becomes more difficult.

The fabrication methods described above require expensive equipment and photolithography or expensive materials for the fabrication of each device, which makes them inaccessible to many research groups. Injection molding of solder[14] or conductive fluids such as phosphate buffered saline[19,37] into microfluidic channels offers an affordable alternative to these methods when electric fields are to be generated in microfluidic devices made from PDMS. However, the electrodes resulting from these methods do not have direct contact with the working fluid which makes them unsuitable for applications that require currents to be passed through the fluid.

A method that overcomes this limitation has recently been demonstrated by Pavesi *et al.*[38] who demonstrated injection molding of a conductive PDMS–carbon nanotube composite with subsequent etching of the thin PDMS walls separating the electrodes from the working fluid. Another approach is to inject liquid metal or metal with a low melting point into the devices, as demonstrated by So *et al.*[20] These methods are affordable compared to the methods presented above. Once a micromold has been fabricated (or purchased), no further cleanroom work or expensive equipment is required for the fabrication of the devices. However, the variety of achievable electrode geometries is rather limited compared to most of the other methods presented above.

The present article introduces an affordable replica molding method for integrating 3D-composite electrodes into microfluidic devices made from PDMS. Compared to the methods mentioned in the preceding paragraph, a greater variety of electrode geometries can be achieved.

2 Integration of 3D-electrodes into microfluidic devices by replica molding

Materials and process overview

The method presented here is based on a dry nanoparticle embedding technique that was recently demonstrated for fabricating magnetic polymer micropillars for MEMS applications.[39] Micromold masters required for fabricating microfluidic devices with integrated 3D electrode structures by replica molding are produced in a cleanroom using standard multilayer SU-8 (MicroChem, Newton, MA, US) photolithography. As these micromolds have a limited lifetime, copies of the mold masters are fabricated from polyurethane (Smooth cast 310, Smooth-on, Easton, PA, US) using the process described in ref. 40 before the replica molding procedure illustrated in Fig. 1 is performed using these copies. Throughout the process, the PDMS (Sylgard 182, Dow Corning, Midland, MI, US) is used in a 10 : 1 (base : hardener) ratio.

In the first step of the fabrication procedure carbon black (CB) nanoparticles (Vulcan XC72R, Cabot, Boston, MA, US) with a primary particle size of 150–180 nm are applied to the mold in dry form using a tongue depressor. This step should be performed thoroughly in order to decrease spatial variation of the electrode conductivity. As shown in Fig. 1(a), this leaves CB particles not only in the holes and groves that will later result in the electrodes of the device, but also everywhere else on the

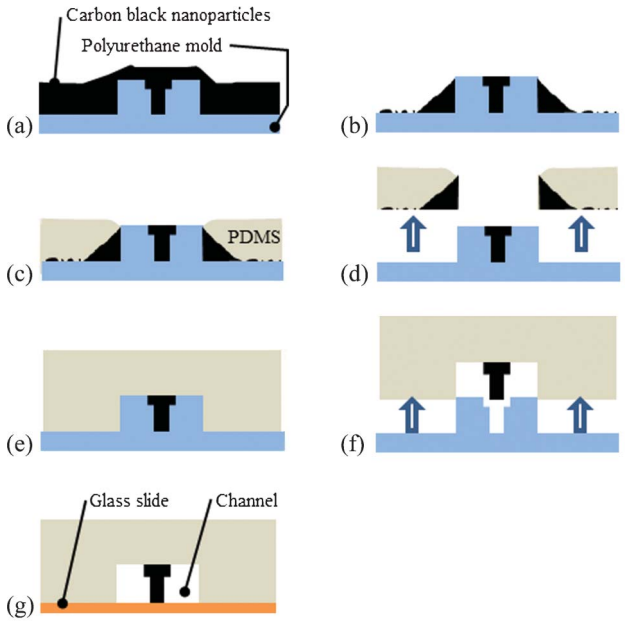

Fig. 1 Process overview: (a) Apply CB particles to the mold using a tongue depressor. (b) Remove excess particles using a cotton applicator. (c) Cast the remaining excess particles into PDMS. (d) Cure and remove the thin layer of PDMS. (e) Cover the mold with PDMS and cure at room temperature overnight. (f) Peel the PDMS. (g) Bond the PDMS to a glass slide or to another fluidic layer to seal the channel.

mold. The excess CB particles are removed in two steps: in the first step, excess particles are removed as much as possible using a cotton applicator (Fig. 1(b)). The remaining excess particles are cast into PDMS as shown in Fig. 1(c). The micromolds incorporate barriers surrounding the main features, as shown in Fig. 2(a). The barriers facilitate the casting process as controlled volumes of uncured PDMS can be applied to the mold using a micropipette until the PDMS film fills the whole area within the barrier, as shown in Fig. 2(b) for a clean wafer. The thin layer is cured in an oven at 65 °C for 30 min before the rest of the wafer is covered with a thin layer of PDMS using a tongue depressor. The mold is put back in the oven for 1 h until the PDMS is cured. The PDMS containing the excess CB particles is then peeled off the mold using plastic tweezers with a flat tip (Lerloy, Los Angeles, CA, US) (Fig. 1(d)). After this step, only the regions on the mold that will later result in the electrodes are filled with CB particles. Another batch of PDMS is mixed and degassed in a desiccator for 15 min before pouring it on the mold. Without further degassing, the PDMS covered mold is left at room temperature for 10 h, as shown in Fig. 1(e). During this time, the uncured PDMS enters the porous medium formed by the CB particles on the mold. The PDMS fills the space between the CB-particles and cures to form the CB–PDMS composite. After an additional hour of curing in an oven at 65 °C, the PDMS device containing 3D-composite electrode structures is peeled off the wafer and fluidic inlet ports are produced using a 0.5 mm Uni-Core hole punch (Harris (Whatman, Maidstone UK). The electrical chip-to-world connections are prepared by punching holes in regions 4 and 5 (Fig. 2(a)) of the PDMS device using a 2.5 mm hole punch. A more detailed description of the chip-to-world connections

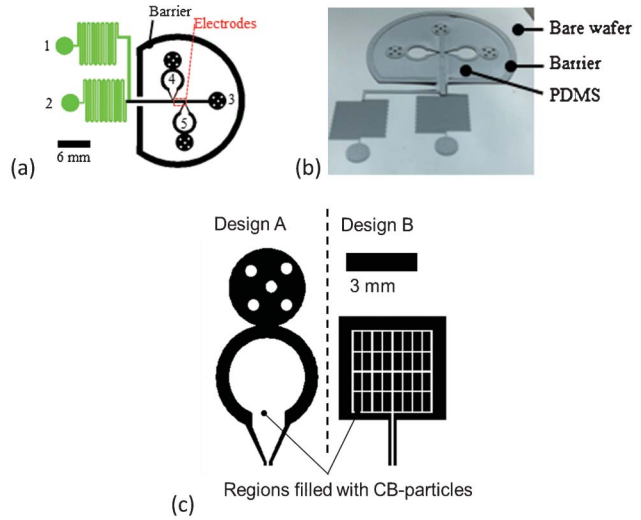

Fig. 2 (a) General device layout: The barrier surrounding the main features facilitates the fabrication step shown in Fig. 1(c); 1, 2 and 3 are fluidic inlet and outlet ports; 4 and 5 indicate the locations for the electrical chip-to-world connections. (b) Silicon substrate with SU-8 mold structures after the application of PDMS with a pipette to remove the excess CB. (c) Design A (left) and design B (right) for the electrical chip-to-world connections.

follows in the next sub section. Finally, the PDMS device is sealed by bonding it to a glass slide using oxygen plasma bonding.[41]

Electrical chip-to-world connections

All microfluidic devices containing integrated electrodes fabricated in this work have the general layout shown in Fig. 2(a). Before the PDMS devices are sealed by bonding them to a glass slide, the device is prepared for making electrical chip-to-world connections by punching holes into the PDMS device in regions 4 and 5. These regions are filled with CB–PDMS composite connecting to the electrodes in the microfluidic channels. After the PDMS has been bonded to a glass slide by oxygen plasma bonding, the punched holes are filled with a CB–PDMS composite using a 10 ml BD-plastic syringe and a flat needle tip (Nordson EFD, Robbinsville, NJ, US). The CB–PDMS composite with a CB loading of 18 wt% was pre-mixed by hand for 15 min using a spatula. CB loadings above 18 wt% result in a material that is too viscous for injection. In order to achieve a good contact with the CB–PDMS composite already present in regions 4 and 5, the needle tip is to be inserted all the way down to the glass slide before the injection is started. If required, the top side of the device can be cleaned from the CB–PDMS composite after injection using a razor blade. Stranded wires are then inserted into the holes filled with CB–PDMS composite and the device is placed into an oven at 65 °C for one hour. Storing the pre-mixed CB–PDMS composite in the 10 ml syringe in a freezer at −20 °C slows the curing process of the composite so that the same mixture can be used for up to two months.

The design of regions 4 and 5 in Fig. 2(a) was found to be somewhat challenging as it is difficult to fill these large circular cavities of the mold with a continuous thin layer of CB particles. Although it was still possible to produce functional electrical chip-to-world connections with design A, shown in Fig. 2(a), the improved design B for the connection region on the mold shown in Fig. 2(c) overcomes this problem. Here, the CB particles fill a network of narrow channels instead of a single large circular cavity. This design was employed for the devices that were used for the characterization of the electrical properties of the composite PDMS, which will be presented in the next section.

The realization of the electrical chip-to-world connections introduces dead end microchannels along the sides of the lead connections from the contact areas 4 and 5 to the electrodes in the channels. If the dead end microchannels cannot be tolerated, they can be closed by injecting CB–PDMS composite with a CB loading of 18 wt% into the additional fluidic inlet ports near regions 4 and 5 in Fig. 2(a) after the device has been bonded to a glass slide. Fig. 3(g) shows the result from this procedure for the top connection compared to the unfilled dead end channels next to the bottom connection of the device.

Achievable geometries and limitations

A great variety of electrode geometries can be demonstrated and, over a wide range, the achievable electrode geometry is only limited by the resolution and by the aspect ratio that can be

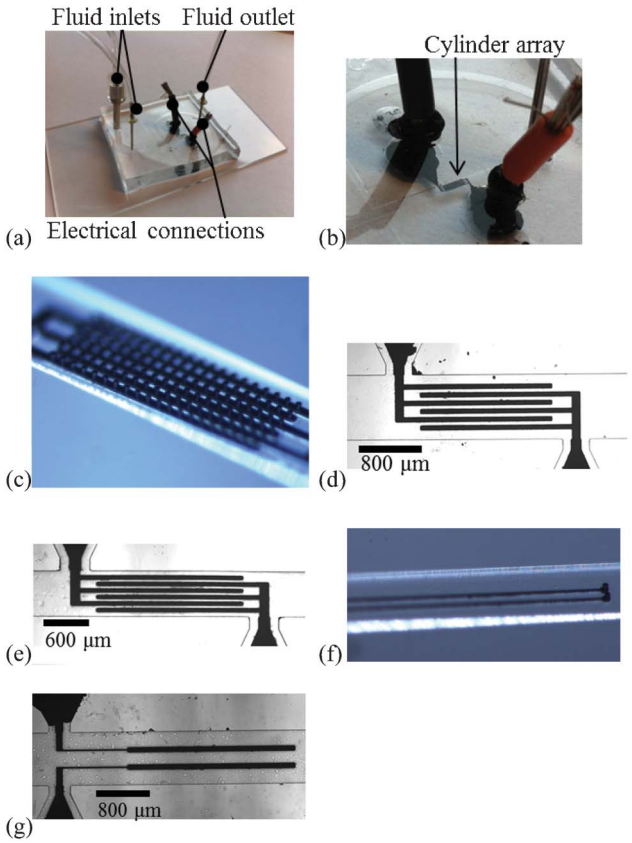

Fig. 3 (a) and (b) Image of a device containing an array of conductive cylinders (black) with a diameter of 40 µm and a height of 45 µm connected to leads with a 60 µm × 35 µm cross section in an 800 µm wide and 80 µm high channel as shown in (c). (d) and (e) Top-view of the cylinder array with (e) 40 µm and (e) 20 µm gaps between the leads. (f) Cylinders with the same dimensions as in (c) connected to 20 µm × 20 µm leads. (g) Two 80 µm wide and 80 µm high plate electrodes connected to leads with a 30 µm × 20 µm cross section.

achieved by the photolithography process utilized for the fabrication of the mold. Fig. 3 shows an image of a complete device as well as different electrode geometries that were fabricated using the process described above. The limitations for the achievable electrode geometries are discussed below:

Electrode aspect ratio. It was found that there is a lower bound to the achievable electrode aspect ratio $ar = H/W$, where H and W represent the minimum height and the maximum width of the electrode respectively. For low $ar < 1$, the CB-particles do not stay in the centers of the holes and groves of the mold during the application of the particles. For large aspect ratios, the application of the CB particles using the tongue depressor should be repeated a few times to ensure that the particles fill the holes and groves of the mold.

Total channel height. It is expected that there is a lower bound to the achievable channel height H as the removal of the layer embedding the excess CB particles (Step (d) in Fig. 1) becomes increasingly difficult with decreasing layer thickness. The limit for the minimum total channel height was not determined in this work. The smallest channel height employed in this work was $H_{min} = 70$ μm, for which peeling of the thin PDMS layer did not pose a problem.

Lifetime of a mold. The removal of the layer embedding the excess CB particles (step (d) in Fig. 1) was more difficult for molds that were used multiple times. We believe that the application of the nanoparticles can roughen the surface of the micromold and hence make the removal of the thin layer of PDMS more difficult. A single polyurethane mold was successfully reused between 3 and 8 times before a new copy of the mold was needed.

Electrical properties of the CB–PDMS composite material

The electrical properties of the conductive composite PDMS were characterized using the devices and circuits shown in Fig. 4. The devices consisting of leads of 1 cm length with a cross section of 100 μm × 93 μm were fabricated using the procedure described in section "Materials and process overview". Design B was employed for the electrical chip-to-world connections, as shown in the upper half of Fig. 4(a). Holes were punched in the array of narrow channels and pre-mixed CB–PDMS composite with a CB loading of 18 wt% was applied using a syringe. Wires were then added and the device was put in the oven at 65 °C for curing. The devices were connected to an E3631A power supply (Agilent, Santa Clara, CA, US) which supplied the constant voltage $V_s = 25$ V. The currents I_1 and I_2 and the potentials V_1–V_6 were measured using a U1252 Multimeter (Agilent). The lead resistances R and R_1–R_5 as well as the contact resistances R_{c1} and R_{c2} were then calculated from Ohm's law. The mean conductivity and the corresponding standard deviation determined from 33 lead resistance measurements was 16.74 S m^{-1} and 8.1 S m^{-1} respectively. The mean and the standard deviation of the contact resistance determined from six measurements were 2.44 kΩ and 1.61 kΩ respectively.

The conductivity of manually pre-mixed CB–PDMS composites has previously been investigated for different CB loadings using macroscopic samples.[29,35] The authors report a conductivity close to the one measured in the present work for CB loadings of 25 wt%[35] and above.[29] For CB-loadings greater than 25 wt%, integration of CB–PDMS composites into microsystems using standard photolithography methods becomes difficult as the uncured composite becomes brittle at these concentrations.[29]

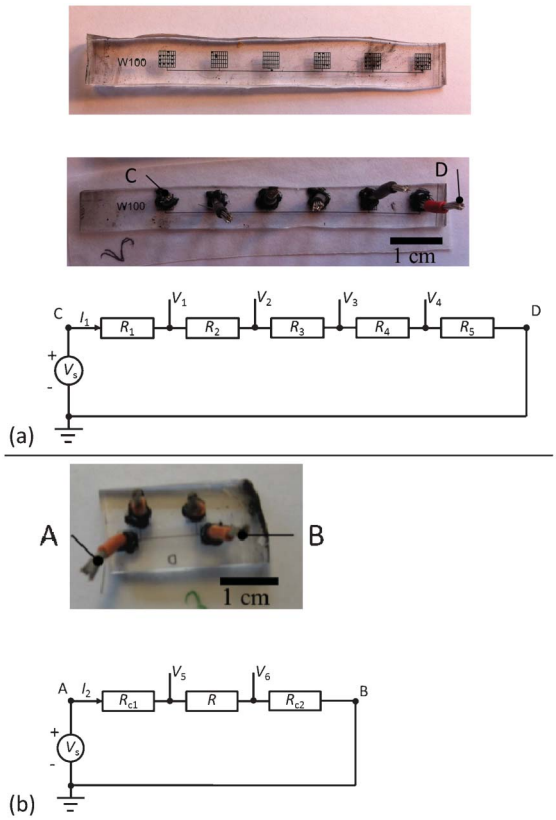

Fig. 4 Devices and corresponding circuits used for characterizing the electrical properties of the CB–PDMS composite.

Additionally, impedance measurements were performed on the samples shown in Fig. 4(b) using a 4294A Precision Impedance Analyzer (Agilent) in the shielded four-terminal (4T) configuration.[42] The impedance was measured between port A and B shown in Fig. 4(b). Impedance data for three samples with lead resistances ranging from close to the mean resistance (Sample 1) to close to the maximum measured resistance (Sample 3) are shown in Fig. 5. The magnitude of the impedance was normalized with respect to the magnitude of the impedance at $f = 40$ Hz where $|Z|_{40Hz} = 73$ kΩ, 109 kΩ and 244 kΩ for sample 1, 2 and 3, respectively. All samples show resistive behavior for frequencies below 1 MHz, which makes the CB–PDMS composite suitable for AC-electrokinetic applications. At high frequencies $f > 10$ MHz, cross talk between the cables of the measurement fixture seemed to affect the measurement results.

3 Example application to particle concentration *via* AC-dielectrophoresis

A common application for electrodes in microfluidic devices is the on-chip concentration of particles.[4,5,43–50] In this section, a device for concentrating particles is presented as a potential

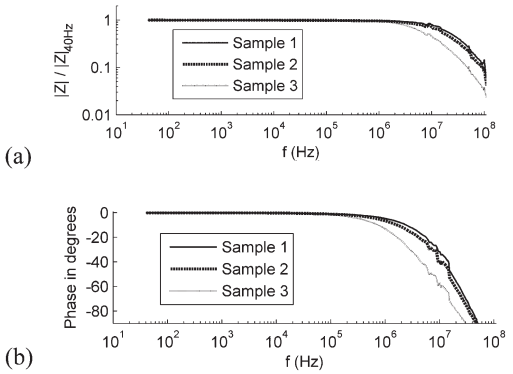

Fig. 5 Impedance data for three devices with different CB–PDMS lead resistances: (a) Normalized magnitude of the impedance. (b) Phase data.

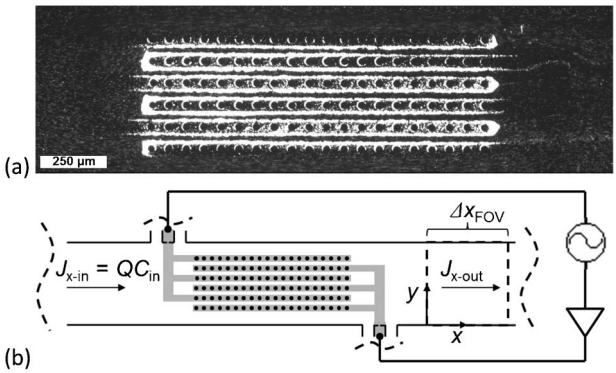

Fig. 6 (a) Microscopic image of particles (appear bright) accumulating in the concentration region due to AC-dielectrophoresis. (b) Experimental setup: A suspension with solid concentration C_{in} is driven through a cylinder array at a flow rate Q provided by a syringe pump. The electrodes are connected to a function generator that produces a sinusoidal voltage signal and a voltage amplifier. While particles accumulate in the concentration region, the average outgoing particle flux $J_{x\text{-out}}$ is measured using fluorescence microscopy.

application for the fabrication process and to demonstrate the functionality of the resulting devices.

Different electrokinetic phenomena have been utilized for concentrating particles in microfluidic devices. Examples include electrohydrodynamic phenomena,[4,46,49] AC-dielectrophoresis,[5,45,47,51–53] and a combination of AC-electroosmotic pumping and dielectrophoresis.[50] The device presented in the present work utilizes AC-dielectrophoresis (DEP)[54,55] for concentrating polystyrene particles.

An isolated and perfectly spherical particle that is immersed in a flow field $\vec{U}_0$ and homogeneously polarized (dipole approximation) by an inhomogeneous AC-electric field with spatially constant phase migrates with the velocity

$$\vec{U} = \vec{U}_{DEP} + \vec{U}_0 = \vec{K}\mathrm{Re}(\tilde{f}_{CM})(U_{rms})^2 + \vec{U}_0 \qquad (1)$$

where $\vec{K} = \vec{f}(\varepsilon_0\varepsilon_m, a, \Psi)$, ε_0, is the electric constant, ε_m is the permittivity of the liquid phase surrounding the particle, a is the particle radius, Ψ is a set of parameters describing the electrode geometry, $\mathrm{Re}(\tilde{f}_{CM})$ is the real part of the Clausius Mossotti factor, U_{rms} is the root mean square value of the electrical potential applied to the electrodes. A more detailed derivation of eqn (1) can be found in the supplementary material to this article.

Particle concentration can be achieved through negative DEP[45,51,52] and through positive DEP.[5,45,47,53] The general strategy behind these approaches is to generate an electric field such that $\vec{U} = \vec{0}$ for the given flow field $\vec{U}_0$. The particle concentration device presented in this work concentrates polystyrene particles *via* positive DEP. Polystyrene particles in low conductivity liquid medium are expected to experience positive DEP for frequencies up to several megahertz.[56,57]

The device layout is shown in Fig. 2(a) and a complete device is shown in Fig. 3(a) and (b). The electrodes consist of parallel rows of cylinders, where each row is connected to a lead as shown in Fig. 3(c)–(e), and neighboring rows have a different electric potential. Application of an AC-potential U_{rms} to the electrodes establishes an inhomogeneous AC-electric field $\vec{E}$ in the electrode region and particles accumulate in regions of maximum field intensity, as shown in Fig. 6(a) (high field concentration near sharp corners).

The performance of the particle concentrator was evaluated experimentally by determining the flux J_{dep} of trapped particles. The leads were connected to a FG3C function generator (Meterman, Everett, WA, US) and to a 9400 wideband amplifier (Taber Electronics, Tel Hanan, Israel), as shown in the schematic of the experimental setup in Fig. 6(b). During an experiment a suspension of fluorescent polystyrene particles (Thermo Scientific, Waltham, MA, US) with a mean diameter of d = 1 μm and with the volume concentration of particles of C_{in} = 0.0075 vol% was driven through the device at a flow rate Q using a KDS200 syringe pump (KD scientific, Holliston, MA, USA). The region downstream of the cylinder array was observed using a TE-2000e epifluorescence microscope (Nikon, Tokyo, Japan) and a 5× objective lens (the depth of view exceeded the channel height). Before the experiments, the relationship $C_{out}(I(x_i,y_j,t_k))$ between particle concentration and fluorescence intensity was determined through calibration. During an experiment, greyscale images $I(x_i,y_j,t_k)$ of the field of view (FOV) downstream of the cylinder array were recorded with a frame rate of 1 Hz using an Imager sCMOS camera (LaVision, Ypsilanti, MI, US). Assuming that the particle concentration is uniform over the depth of the channel and that the fluid velocity is uniform, the approximate average outgoing particle flux was calculated from

$$J_{x-out}(t_k) = \frac{QA_{px}}{\Delta x_{FOV} W}\sum_i \sum_j C_{out}(I(x_i,y_i,t_k)), \qquad (2)$$

where Δx_{FOV} = 1 mm is the length of the FOV, W is the channel width and A_{px} is the area of one pixel (the summation is performed over the FOV). The particle trapping rate $J_{dep}(t)$ was then calculated from the difference between incoming particle flux and outgoing particle flux.

Fig. 7(a) shows trapping rates for U_{rms} = 20 V, 10 V and 5 V at a flow rate of Q = 1 μl min^{-1}. An apparent increase of the trapping rates over time is observed after the field is switched on at t = 0 s until they reach a maximum. This is a result of the suspension, which was present in the channel downstream of the cylinder array before the field was switched on, passing through the FOV. The particle trapping rate then decreases over time as more particles accumulate in the cylinder array. In a control test with U_{rms} = 0 V, no measurable particle trapping rate was

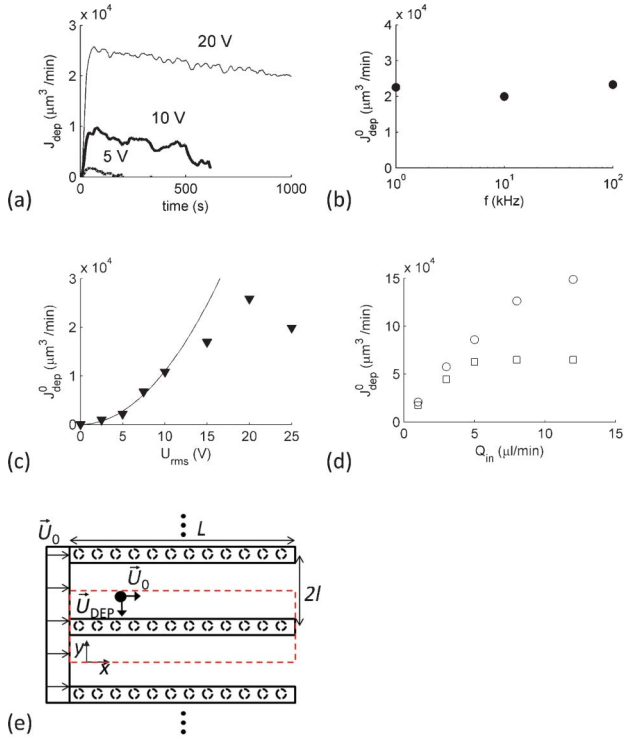

Fig. 7 (a) Deposition rates for U_{rms}= 20 V (top), 10 V (middle) and 5 V (bottom) at Q = 1 µl min^{-1}, C_{in} = 0.0075 wt% and f = 100 kHz. (b) Initial deposition rate at Q = 1 µl min^{-1} for three frequencies at U_{rms} = 20 V and (c) for different input voltages U_{rms} at f = 100 kHz. The solid line represents the fit $J^0_{dep} = a(U_{rms})^2$ with a = 109.9 µm^3 min^{-1} V^{-2}. (d) Initial deposition rate as a function of flow rate for the two input voltages U_{rms} = 15 V (squares) and U_{rms} = 25 V (circles) at f = 100 kHz. (e) Schematic of the cylinder array.

observed. The repeatability of the results was tested by performing three consecutive trapping experiments. The maximum trapping rates and volumes of trapped particles obtained from the three consecutive experiments differed by less than 3% and 8%, respectively, while all three curves showed an initial increase of the trapping rate with an identical slope.

In the following, the focus was set on the initial trapping rates J^0_{dep}. The initial trapping rates were determined by extrapolating the trapping rates to $t = t_{transit}$, where $t_{transit}$ is the average time required for a particle to travel from the beginning of the cylinder array to the end of the FOV ($t_{transit}$ = 22 s for Q = 1 µl min^{-1}). As shown in Fig. 7(b), the initial trapping rates are independent of the frequency of the applied potential over the investigated frequency range of 1 kHz $< f <$ 100 kHz. In this frequency range, the Clausius Mossotti factor and hence the DEP-force can be expected to be independent of frequency.[56,57] Further experiments were conducted at f = 100 kHz. The influence of the applied potential on the initial trapping rates for Q = 1 µl min^{-1} is shown in Fig. 7(c). At low applied potentials $U_{rms} < 10$ V, the trapping rates follow a quadratic increase with the applied potential. For large potentials $U_{rms} > 15$ V, the trapping rates seem to become independent of the applied potential. The influence of the flow rate on the initial trapping rates at two different applied potentials is shown in Fig. 7(d). The trapping rates show a linear increase with the flow rate for low flow rates and they saturate at larger flow rates. With increasing applied potential, the trapping rates saturate at a higher flow rate. The observed effects of flow rate and applied potential on the initial trapping rate suggest that the trapping rates are governed by convection and DEP.

The initial trapping rate per cylinder row can be captured with a simple model that explains the roles of convection and DEP on the initial trapping rates qualitatively. According to eqn (1), the velocity of a particle in the concentration region consists of a convective part $\vec{U}_0$ and of a migration part $\vec{U}_{DEP}$. In the device presented in this work, convection carries particles through the cylinder array while DEP causes particles to migrate toward the electrode walls. The simple model presented here is based on the assumption that every particle arriving at $y = l$ will be trapped, as shown in Fig. 7(e), with the distance between rows 2l. It can be distinguished between two limiting cases. In the first case every particle that enters the concentrator region will be trapped so that the flow rate is the rate limiting factor. In the second case, not every particle will reach the electrode before they exit the concentrator region. In this case DEP is the rate limiting factor. In order to arrive at simple equations that demonstrate the effect of the flow rate and applied potential on the initial deposition rate, two additional assumptions are made:

1) The flow field $\vec{U}_0 = U_0\vec{e}_x$ is uniform ($\vec{e}_x$ represents unit base vector)

2) Particle migration towards the cylinder row occurs only in y-direction and with constant velocity $\vec{U}_{DEP} = U_{DEP}\vec{e}_y$, where $U_{DEP} = K\mathrm{Re}(\tilde{f}_{CM})U^2_{rms}$.

For case 1, these assumptions lead to the expression for the initial deposition rate per cylinder row

$$\bar{J}^0_{dep1} = mC_{in}\bar{Q}, \text{ for } \bar{Q} < 2K\mathrm{Re}(\tilde{f}_{CM})LH_cU^2_{rms}, \quad (3)$$

where $\bar{Q} = U_0 2lH_c$ is the flow rate between neighboring cylinder rows, H_c is the channel height, L is the length of a cylinder row and m = 1 or 0.5 for an inner and an outer cylinder row, respectively. The model predicts both the linear increase of the trapping rate with the flow rate, as observed in Fig. 7(d), and the frequency independence of the trapping rate as seen in Fig. 7(b). The trapping rate becomes independent of the flow rate for $\bar{Q} \geqslant 2K\mathrm{Re}(\tilde{f}_{CM})LH_cU^2_{rms}$. In this case, DEP becomes the rate limiting step and the trapping rate

$$\bar{J}^0_{dep2} = 2H_cLmC_{in}K\mathrm{Re}(\tilde{f}_{CM})U^2_{rms}, \quad \text{for } \bar{Q} \geqslant 2K\mathrm{Re}(\tilde{f}_{CM})LH_cU^2_{rms} \quad (4)$$

scales quadratically with the applied potential, as observed in Fig. 7(c). The trapping rate is linear to the Clausius Mossoti function which can be expected to be independent of frequency in the investigated range.[56,57] The model qualitatively explains the observed effect of the applied potential U_{rms}, flow rate Q, and frequency f on the initial trapping rate for a given electrode geometry. Furthermore, it is expected that it captures the effect of the length of the cylinder rows L on the capture rate in good approximation.

4 Conclusions

A method for integrating 3D-electrode structures into microfluidic devices made from polydimethylsiloxane was demonstrated. The method has several advantages over previous methods. It is comparably affordable and does not rely on expensive equipment once a micromold master has been fabricated. Great flexibility in achievable electrode geometries was demonstrated. No aligning between an electrode layer and a fluidic layer is required and the devices are leakage free. The conductivity of the CB–PDMS composite obtained through the dry-embedding process was found to be equal to or higher than the conductivity of comparable composites that were mechanically mixed. Particles made from materials with higher bulk conductivity could be used in case a higher conductor conductivity is required. The fabrication process yields devices that are suitable for electrokinetic applications as demonstrated with a device for the concentration of polystyrene particles *via* AC-DEP.

Acknowledgements

This work was supported by the Natural Science and Engineering Research Council (NSERC) of Canada through the Special Research Opportunity program.

References

1 P. S. Dittrich, K. Tachikawa and A. Manz, *Anal. Chem.*, 2006, **78**, 3887–3907.
2 S. Haeberle and R. Zengerle, *Lab Chip*, 2007, **7**, 1094–1110.
3 D. Erickson and D. Q. Li, *Anal. Chim. Acta*, 2004, **507**, 11–26.
4 K. H. Bhatt, S. Grego and O. D. Velev, *Langmuir*, 2005, **21**, 6603–6612.
5 N. Gadish and J. Voldman, *Anal. Chem.*, 2006, **78**, 7870–7876.
6 M. Durr, J. Kentsch, T. Muller, T. Schnelle and M. Stelzle, *Electrophoresis*, 2003, **24**, 722–731.
7 N. Demierre, T. Braschler, P. Linderholm, U. Seger, H. van Lintel and P. Renaud, *Lab Chip*, 2007, **7**, 355–365.
8 R. S. Martin, A. J. Gawron, S. M. Lunte and C. S. Henry, *Anal. Chem.*, 2000, **72**, 3196–3202.
9 M. H. Oddy, J. G. Santiago and J. C. Mikkelsen, *Anal. Chem.*, 2001, **73**, 5822–5832.
10 H. Lu, M. A. Schmidt and K. F. Jensen, *Lab Chip*, 2005, **5**, 23–29.
11 M. B. Fox, D. C. Esveld, A. Valero, R. Luttge, H. C. Mastwijk, P. V. Bartels, A. van den Berg and R. M. Boom, *Anal. Bioanal. Chem.*, 2006, **385**, 474–485.
12 A. M. Skelley, O. Kirak, H. Suh, R. Jaenisch and J. Voldman, *Nat. Methods*, 2009, **6**, 147–152.
13 N. Pamme, *Lab Chip*, 2006, **6**, 24–38.
14 A. C. Siegel, S. S. Shevkoplyas, D. B. Weibel, D. A. Bruzewicz, A. W. Martinez and G. M. Whitesides, *Angew. Chem., Int. Ed.*, 2006, **45**, 6877–6882.
15 R. Pal, M. Yang, R. Lin, B. N. Johnson, N. Srivastava, S. Z. Razzacki, K. J. Chomistek, D. C. Heldsinger, R. M. Haque, V. M. Ugaz, P. K. Thwar, Z. Chen, K. Alfano, M. B. Yim, M. Krishnan, A. O. Fuller, R. G. Larson, D. T. Burke and M. A. Burns, *Lab Chip*, 2005, **5**, 1024–1032.
16 B. Stoeber, Z. H. Yang, D. Liepmann and S. J. Muller, *J. Microelectromech. Syst.*, 2005, **14**, 207–213.
17 B. Stoeber, D. Liepmann and S. J. Muller, *Phys. Rev. E: Stat., Nonlinear, Soft Matter Phys.*, 2007, **75**, 4.
18 W. Ebina, A. C. Rowat and D. A. Weitz, *Biomicrofluidics*, 2009, **3**, 034104.
19 M. B. Sano, J. L. Caldwell and R. V. Davalos, *Proc. IEEE Engn Med & Biol Soc (EMBS)*, 2011, 8384–8387.
20 J. H. So and M. D. Dickey, *Lab Chip*, 2011, **11**, 905–911.
21 G. Mottet, J. Villemejane, L. M. Mir and B. Le Pioufle, *Journal of Micromechanics and Microengineering*, 2010, **20**, 047001.
22 J. Voldman, M. Toner, M. L. Gray and M. A. Schmidt, *J. Electrost.*, 2003, **57**, 69–90.
23 L. Wang, L. A. Flanagan, N. Li Jeon, E. Monuki and A. P. Lee, *Lab Chip*, 2007, **7**, 1114–1120.
24 C. Iliescu, G. L. Xu, V. Samper and F. E. H. Tay, *J. Micromech. Microeng.*, 2005, **15**, 494–500.
25 C. L. Wang, G. Y. Jia, L. H. Taherabadi and M. J. Madou, *J. Microelectromech. Syst.*, 2005, **14**, 348–358.
26 B. Y. Park and M. J. Madou, *Electrophoresis*, 2005, **26**, 3745–3757.
27 J. W. Choi, S. Rosset, M. Niklaus, J. R. Adleman, H. Shea and D. Psaltis, *Lab Chip*, 2010, **10**, 783–788.
28 J. Zhou, D. A. Khodakov, A. V. Ellis and N. H. Voelcker, *Electrophoresis*, 2012, **33**, 89–104.
29 A. L. Deman, M. Brun, M. Quatresous, J. F. Chateaux, M. Frenea-Robin, N. Haddour, V. Semet and R. Ferrigno, *J. Micromech. Microeng.*, 2011, **21**, 095013.
30 C. X. Liu and J. W. Choi, *J. Micromech. Microeng.*, 2009, **19**, 085019.
31 X. Niu, M. Zhang, S. Peng, W. Wen and P. Sheng, *Biomicrofluidics*, 2007, **1**, 044101.
32 N. Lewpiriyawong, C. Yang and Y. C. Lam, *Electrophoresis*, 2010, **31**, 2622–2631.
33 H. S. Chuang and S. Wereley, *J. Micromech. Microeng.*, 2009, **19**, 045010.
34 H. Li, C. X. Luo, H. Ji, Q. Ouyang and Y. Chen, *Microelectron. Eng.*, 2010, **87**, 1266–1269.
35 X. Niu, S. Peng, L. Liu, W. Wen and P. Sheng, *Adv. Mater.*, 2007, **19**, 2682–2686.
36 S. P. Rwei, F. H. Ku and K. C. Cheng, *Colloid Polym. Sci.*, 2002, **280**, 1110–1115.
37 M. B. Sano, J. L. Caldwell and R. V. Davalos, *Biosens. Bioelectron.*, 2011, **30**, 13–20.
38 A. Pavesi, F. Piraino, G. B. Fiore, K. M. Farino, M. Moretti and M. Rasponi, *Lab Chip*, 2011, **11**, 1593–1595.
39 F. Khademolhosseini and M. Chiao, *Proc IEEE Micro Electro Mechanical Systems*, 2012, 212–215.
40 S. P. Desai, D. M. Freeman and J. Voldman, *Lab Chip*, 2009, **9**, 1631–1637.
41 K. Haubert, T. Drier and D. Beebe, *Lab Chip*, 2006, **6**, 1548–1549.
42 *Agilent Impedance Measurement Handbook*. Agilent, 2009.
43 T. Muller, A. Gerardino, T. Schnelle, S. G. Shirley, F. Bordoni, G. DeGasperis, R. Leoni and G. Fuhr, *J. Phys. D: Appl. Phys.*, 1996, **29**, 340–349.
44 E. B. Cummings, *IEEE Eng. Med. Biol. Mag.*, 2003, **22**, 75–84.
45 H. B. Li, Y. N. Zheng, D. Akin and R. Bashir, *J. Microelectromech. Syst.*, 2005, **14**, 103–112.
46 M. Felten, W. Staroske, M. S. Jaeger, P. Schwille and C. Duschl, *Electrophoresis*, 2008, **29**, 2987–2996.
47 Y. K. Cho, T. H. Kim and J. G. Lee, *J. Micromech. Microeng.*, 2010, **20**, 065010.
48 M. D. Vahey and J. Voldman, *Lab Chip*, 2011, **11**, 2071–2080.
49 M. Boettcher, S. Schmidt, A. Latz, M. S. Jaeger, M. Stuke and C. Duschl, *J. Phys.: Condens. Matter*, 2011, **23**, 324101.
50 E. M. Melvin, B. R. Moore, K. H. Gilchrist, S. Grego and O. D. Velev, *Biomicrofluidics*, 2011, **5**, 034113.
51 B. H. Lapizco-Encinas, B. A. Simmons, E. B. Cummings and Y. Fintschenko, *Electrophoresis*, 2004, **25**, 1695–1704.
52 B. H. Lapizco-Encinas, R. V. Davalos, B. A. Simmons, E. B. Cummings and Y. Fintschenko, *J. Microbiol. Methods*, 2005, **62**, 317–326.
53 C. Iliescu, G. Xu, F. C. Loe, P. L. Ong and F. E. H. Tay, *Electrophoresis*, 2007, **28**, 1107–1114.
54 H. Morgan and N. Green, in *AC Electrokinetics: Colloids and Nanoparticles*, Research Studies Press, 2003.
55 R. Pethig, *Biomicrofluidics*, 2010, **4**, 022811.
56 N. G. Green and H. Morgan, *J. Phys. Chem. B*, 1999, **103**, 41–50.
57 I. Ermolina and H. Morgan, *J. Colloid Interface Sci.*, 2005, **285**, 419–428.

